

Gravitational wave signatures from an extended inert doublet dark matter model

Avik Paul¹, Biswajit Banerjee², Debasish Majumdar³

*Astroparticle Physics and Cosmology Division,
Saha Institute of Nuclear Physics, HBNI,
1/AF Bidhannagar, Kolkata 700064, India*

Abstract

We consider a particle dark matter model by extending the scalar sector of the Standard Model by an additional $SU(2)$ scalar doublet which is made “inert” (and stable) by imposing a discrete Z_2 symmetry under which the additional scalar doublet is odd (and the SM is even) and it does not develop any vacuum expectation value (VEV). The lightest inert particle (LIP) of this inert doublet model (IDM) can be a viable candidate for Dark Matter. The IDM model is further extended by an additional singlet scalar which is also even under Z_2 and develop a VEV on spontaneous symmetry breaking. This additional scalar singlet mixes with SM Higgs and on diagonalisation of the mass matrix two CP even scalar eigenstates are obtained one of which is attributed to the physical Higgs (with mass 125 GeV). The LIP is the dark matter candidate in the extended model. For such a particle dark matter model we explore the first order electroweak phase transition and consequent production of Gravitational Waves (GW) at that epoch of the early Universe and calculate the frequencies for such waves. We then investigate the detection possibilities of such GWs at the future space borne primordial GW detectors such as eLISA, BBO, ALIA, DECIGO, U-DECIGO and aLIGO.

¹email: avik.paul@saha.ac.in

²email: biswajit.banerjee@saha.ac.in

³email: debasish.majumdar@saha.ac.in

1 Introduction

Recently, with the detection of a gravitational wave (GW) event [1, 2] from a black hole binary merger with the Laser Interferometer Gravitational-Wave Observatory (LIGO) the era of GW-astronomy has begun. The production of GW can also be associated with several other different mechanisms such as topological defects of the domain walls and cosmic strings [3], inflationary quantum fluctuations [4], preheating [5], first-order phase transitions in the early Universe [6, 7], etc. In this work, we explore production of GW from the first-order phase transitions in the early Universe for a proposed dark matter particle physics model that is constructed by simple extension of Standard Model (SM) by an inert doublet and a scalar singlet. Also a strong first order electroweak phase transition helps to explain electroweak baryogenesis. It is to be noted that the first order cosmological phase transition originates from the bubble nucleation of a true vacuum state at a temperature known as the nucleation temperature at which the probability for a single bubble to nucleate within the horizon volume is of the order one. Initially, the bubbles are considered to have all possible shapes with different surface tension and internal pressure. The bubbles with the size just large enough for avoiding collapse are considered as a critical bubble. The bubbles which are smaller than the critical bubble tend to collapse whereas the larger bubbles tend to expand due to the pressure difference between the false and true vacua. During the collisions, the bubbles cannot retain their spherical symmetry which initiates phase transitions and as a result, gravitational waves are produced. The details of the GW production mechanisms are discussed in [8]-[22]. The GWs are produced from the strong first-order electroweak phase transition mainly by the following three mechanisms: bubble collisions [8]-[13], sound waves in the hot plasma [14]-[17] and magnetohydrodynamic turbulence of bubbles [18]-[22] in the early Universe.

The electroweak phase transition as explained by SM of particle physics initiated by spontaneous symmetry breaking through Higgs mechanism when acquire a vacuum expectation value (VEV) in a smooth crossover and not a first order phase transition [23]-[25]. However extension of SM by adding scalar singlet field or a Higgs like doublet can induce strong first order phase transitions. The phase transitions can be of two types: a) a one-step process, which involves only initial and final phases and b) a two or multi-step processes, which involves one or more intermediate phases along with the initial and final phases [26]-[30]. In order to explore the gravitational wave production from the first-order phase transition, many authors have considered different types of particle dark matter (DM) models [31]-[38]. So far, different types of particle candidate of dark matter have been proposed such as Weakly Interacting Massive Particles (WIMPs) [39]-[42], Febbly Interating Massive Particles (FIMPs) [43, 44], Axions [45]-[47], neutralino [48], Fuzzy dark matter [49, 50], Kaluza Klein dark matter [51], from extra dimensional models etc.

In this work, we extend the SM by adding an extra Higgs doublet and a real singlet scalar. The added doublet is an inert doublet [52]-[58] in the sense that it does not have any direct coupling with fermion. A Z_2 symmetry is imposed to make it stable. The lightest stable inert particle is attributed to a viable particle candidate of dark matter. The extra singlet scalar mixes with the SM Higgs. This model has already been discussed in previous works [59, 60] but in that work the dark matter mass has been shown to be below the Higgs mass. But in this work we calculate new annihilation channels for this dark matter and showed from the computation of relic densities that the mass of the dark matter in this model can be of low mass (less than Higgs mass) as well as high mass (greater than Higgs mass). We demonstrate that this model in addition to provide a viable particle candidate it induces strong first-order electroweak phase transition. In addition, introducing a new scalar particle increases the degrees of freedom in the thermal plasma and improves the strength of the electroweak phase transition. We constrain the model parameters by using vacuum stability [61], perturbativity, Large Electron-Positron Collider (LEP)[62], Large Hadron Collider (LHC) bounds, PLANCK bound on the DM relic density [63] and limits are given by spin independent direct detection experiments like XENON-1T [64], PandaX-II [65], LUX [66] and DarkSide-50 [67] for obtaining the viable candidate of dark matter. Previous studies on this model have shown that the lightest inert particle is a dark matter candidate in the low mass region ($m_{H_0} \leq 80$ GeV) [59, 60]. As mentioned earlier, in this work, we establish that the particle candidate of dark matter can belong to both low and high mass regions ($m_{H_0} \leq 80$ GeV and $m_{H_0} \geq 80$ GeV). For the latter case, the dark matter particle mainly annihilates into W^+W^- , ZZ , $t\bar{t}$ channels. In this work, the mass of second physical scalar h_2 , appearing due to the interaction between singlet scalar and the SM Higgs has been considered heavier as well as lighter than the Higgs mass. We choose some benchmark points (BPs) from the allowed parameter space to calculate the GW production due to the first order phase transition induced by the present model. We also discuss the detectability of such GW by the future space interferometers such as Big Bang Observer (BBO) [68], Evolved Laser Interferometer Space Antenna (eLISA) [69], Advanced Laser Interferometer Antenna (ALIA) [70], DECi-hertz Interferometer Gravitational wave Observatory (DECIGO) [71], Ultimate-DECIGO (U-DECIGO) [72] and Advanced LIGO (aLIGO) [73].

The paper is organised as follows. In Section 2, we present the extension of an inert doublet model by introducing a singlet scalar and derive the relations between model parameters. In Section 3, we discuss both the theoretical and experimental bounds that we have used to constrain the model parameter space. The calculations of relic density and direct detection cross-section of this extended IDM are given in Section 4. In this section, we also discuss the viable model parameter space from all the constraints mentioned in section 3. In Section 5, we present the finite temperature effective potential to study the electroweak phase transitions in our model.

The production mechanisms of GWs from the first-order phase transitions are also furnished in this section. Finally, we summarize and conclude our work in section 6.

2 The Model

In this work we extend the SM of particle physics by an extra Higgs doublet Φ_I and a real singlet scalar S . While Φ_I is Z_2 even, the SM and the other added scalar singlet is Z_2 odd. The extra doublet does not acquire any VEV, while the added singlet acquires a VEV on spontaneous symmetry breaking and mixes with SM Higgs. The dark matter candidate is the lightest of the two neutral scalars of the inert doublet. The potential of the scalar sector of the model can be expressed as

$$V = m_1^2 \Phi_H^\dagger \Phi_H + m_2^2 \Phi_I^\dagger \Phi_I + \frac{1}{2} m_s^2 S^2 + \lambda_1 \left(\Phi_H^\dagger \Phi_H \right)^2 + \lambda_2 \left(\Phi_I^\dagger \Phi_I \right)^2 + \lambda_3 \left(\Phi_H^\dagger \Phi_H \right) \left(\Phi_I^\dagger \Phi_I \right) + \lambda_4 \left(\Phi_I^\dagger \Phi_H \right) \left(\Phi_H^\dagger \Phi_I \right) + \frac{\lambda_5}{2} \left[\left(\Phi_I^\dagger \Phi_H \right)^2 + \left(\Phi_H^\dagger \Phi_I \right)^2 \right] + \rho_1 \left(\Phi_H^\dagger \Phi_H \right) S + \rho'_1 \left(\Phi_I^\dagger \Phi_I \right) S + \rho_2 \left(\Phi_H^\dagger \Phi_H \right) S^2 + \rho'_2 \left(\Phi_I^\dagger \Phi_I \right) S^2 + \frac{\rho_3}{3} S^3 + \frac{\rho_4}{4} S^4. \quad (1)$$

As mentioned, after spontaneous symmetry breaking SM Higgs field Φ_H acquires a non zero VEV $v = 246.22$ GeV and also the scalar S acquires a VEV v_s . The SM Higgs, additional Higgs doublet and the scalar particle can be represented as

$$\phi_H = \begin{pmatrix} 0 \\ \frac{1}{\sqrt{2}}(v+h) \end{pmatrix}, \quad \phi_I = \begin{pmatrix} H^\dagger \\ \frac{1}{\sqrt{2}}(H_0 + iA_0) \end{pmatrix}, \quad S = v_s + s. \quad (2)$$

After minimise the scalar potential represented in Eq. (1) using the conditions

$$\frac{\partial V}{\partial h} \Big|_{h=s=H^\dagger=H_0=A_0=0} = \frac{\partial V}{\partial s} \Big|_{h=s=H^\dagger=H_0=A_0=0} = 0, \quad (3)$$

we obtain the following relations

$$\begin{aligned} m_1^2 + \lambda_1 v^2 + \rho_1 v_s + \rho_2 v_s^2 &= 0, \\ m_s^2 + \rho_3 v_s + \rho_4 v_s^2 + \frac{\rho_1 v^2}{2v_s} + \rho_2 v^2 &= 0. \end{aligned} \quad (4)$$

The mass matrix of the scalar sector is obtained by calculating the second-order derivatives $\left(\frac{\partial^2 V}{\partial h^2}, \frac{\partial^2 V}{\partial s^2}, \frac{\partial^2 V}{\partial h \partial s}, \frac{\partial^2 V}{\partial H^\pm \partial}, \frac{\partial^2 V}{\partial H_0^2}, \frac{\partial^2 V}{\partial A_0^2} \right)$ of the scalar potential (Eq. (1)) and the elements are

$$m_h^2 = 2\lambda_1 v^2, \quad (5)$$

$$m_s^2 = \rho_3 v_s + 2\rho_4 v_s^2 - \frac{\rho_1 v^2}{2v_s}, \quad (6)$$

$$m_{hs}^2 = \rho_1 v + 2\rho_2 v_s v, \quad (7)$$

$$m_{H^\pm}^2 = m_2^2 + \frac{\lambda_3 v^2}{2} + \rho'_1 v_s + \rho'_2 v_s^2, \quad (8)$$

$$m_{H_0}^2 = m_2^2 + (\lambda_3 + \lambda_4 + \lambda_5) \frac{v^2}{2} + \rho'_1 v_s + \rho'_2 v_s^2, \quad (9)$$

$$m_{A_0}^2 = m_2^2 + (\lambda_3 + \lambda_4 - \lambda_5) \frac{v^2}{2} + \rho'_1 v_s + \rho'_2 v_s^2. \quad (10)$$

As h and s mix, we diagonalise the mass matrix in h, s basis by a unitary matrix U

$$\begin{pmatrix} h_1 \\ h_2 \end{pmatrix} = U \begin{pmatrix} h \\ s \end{pmatrix} = \begin{pmatrix} \cos \theta & -\sin \theta \\ \sin \theta & \cos \theta \end{pmatrix} \begin{pmatrix} h \\ s \end{pmatrix}, \quad (11)$$

to obtain two physical mass eigenstates h_1 and h_2 as

$$h_1 = h \cos \theta - s \sin \theta, \quad h_2 = h \sin \theta + s \cos \theta, \quad (12)$$

where θ is the mixing angle that can be computed from

$$\tan \theta = \frac{y}{1 + \sqrt{1 + y^2}}, \quad \text{where } y = \frac{2m_{h,s}^2}{m_h^2 - m_s^2}. \quad (13)$$

The expressions for the mass eigenstate of the two physical scalars h_1 and h_2 are given as

$$m_{h_1, h_2}^2 = \frac{(m_h^2 + m_s^2)}{2} \pm \frac{(m_h^2 - m_s^2)}{2} \sqrt{1 + y^2}, \quad (14)$$

where the ‘+’ sign is for h_1 and ‘-’ sign is for h_2 . In the present work, h_1 is attributed to the SM like Higgs boson with mass $m_{h_1} = 125.09$ GeV [74] and h_2 is the other scalar with mass m_{h_2} . Here we consider both the cases when $m_{h_2} > m_{h_1}$ and when $m_{h_2} < m_{h_1}$. Considering the coupling λ_5 (in Eq. (1)) to be less than zero, we get H_0 to be the lightest stable particle and the dark matter candidate in our present work. Using Eqs. (4)-(14) we obtain the following relations

$$\lambda_1 = \frac{m_{h_2}^2 \sin^2 \theta + m_{h_1}^2 \cos^2 \theta}{2v^2}, \quad (15)$$

$$\rho_4 = \frac{1}{2v_s^2} \left(m_{h_2}^2 \cos^2 \theta + m_{h_1}^2 \sin^2 \theta + \frac{v^2 \rho_1}{2v_s} - v_s \rho_3 \right), \quad (16)$$

$$\rho_2 = \frac{m_{h_1}^2 - m_{h_2}^2}{4vv_s} \sin 2\theta - \frac{\rho_1}{2v_s}, \quad (17)$$

$$m_1^2 = -\lambda_1 v^2 - \rho_1 v_s - \rho_2 v_s^2, \quad (18)$$

$$m_2^2 = m_{H^\pm}^2 - \frac{\lambda_3 v^2}{2} - \rho'_1 v_s - \rho'_2 v_s^2, \quad (19)$$

$$m_s^2 = -\rho_3 v_s - \rho_4 v_s^2 - \frac{\rho_1 v^2}{2v_s} - \rho_2 v^2. \quad (20)$$

3 Constraints

In this section we will explore various theoretical and experimental bounds are given. These are used to constrain the model parameter space.

3.1 Theoretical Constraints

Vacuum Stability

From the vacuum stability conditions the bounds on the couplings are given as [61]

$$\lambda_1, \lambda_2, \rho_4 > 0, \lambda_3 + 2\sqrt{\lambda_1 \lambda_2} > 0, \quad (21)$$

$$\lambda_3 + \lambda_4 - |\lambda_5| + 2\sqrt{\lambda_1 \lambda_2} > 0, \rho_2 + \sqrt{\lambda_1 \rho_4} > 0, \quad (22)$$

$$\rho'_2 + \sqrt{\lambda_2 \rho_4} > 0, \quad (23)$$

$$2\rho_2\sqrt{\lambda_2} + 2\rho'_2\sqrt{\lambda_1} + \lambda_3\sqrt{\rho_4} + 2\left(\sqrt{\lambda_1\lambda_2\rho_4} + \sqrt{\left(\lambda_3 + 2\sqrt{\lambda_1\lambda_2}\right)\left(\rho_2 + \sqrt{\lambda_1\rho_4}\right)\left(\rho'_2 + \sqrt{\lambda_2\rho_4}\right)}\right) > 0, \quad (24)$$

$$2\rho_2\sqrt{\lambda_2} + 2\rho'_2\sqrt{\lambda_1} + (\lambda_3 + \lambda_4 - \lambda_5)\sqrt{\rho_4} + 2\left(\sqrt{\lambda_1\lambda_2\rho_4} + \sqrt{\left((\lambda_3 + \lambda_4 - \lambda_5) + 2\sqrt{\lambda_1\lambda_2}\right)\left(\rho_2 + \sqrt{\lambda_1\rho_4}\right)\left(\rho'_2 + \sqrt{\lambda_2\rho_4}\right)}\right) > 0. \quad (25)$$

Perturbativity

All the quartic couplings in the tree-level potential (Eq. (1)) must be less than 4π to be consistent with the perturbative conditions.

3.2 Experimental Constraints

Collider Constraints

From the LEP experiment, the bound on the model parameter space is given as [62]

$$m_{H_0} + m_{A_0} > m_Z, \quad m_{H^\pm} > 79.3 \text{ GeV}. \quad (26)$$

The bounds are also obtained from the LHC experimental results. The signal strength of the SM like Higgs h_1 in the present model can be expressed as

$$R_1 = \cos^4 \theta \frac{\Gamma^{\text{SM}}}{\Gamma}, \quad (27)$$

where Γ^{SM} and Γ are the total SM Higgs decay width and total decay width of SM like Higgs boson of mass 125.09 GeV. The expression of Γ can be written as

$$\Gamma = \cos^2 \theta \Gamma^{\text{SM}} + \Gamma^{\text{inv}}, \quad (28)$$

where Γ^{inv} is the invisible Higgs decay width. In our case, there are two possible invisible decay channels of h_1 , one of them is $\Gamma^{\text{inv}}(h_1 \rightarrow H_0 H_0)$ (for $m_{H_0} \leq m_{h_1}/2$, m_{H_0} being the mass of the dark matter particle H_0) and the other one is $\Gamma^{\text{inv}}(h_1 \rightarrow h_2 h_2)$ (for $m_{h_2} \leq m_{h_1}/2$) and they are expressed as

$$\Gamma^{\text{inv}}(h_1 \rightarrow H_0 H_0) = \frac{(g_{h_1 H_0 H_0})^2}{16\pi m_{h_1}} \left(1 - \frac{4m_{H_0}^2}{m_{h_1}^2}\right)^{1/2}, \quad (29)$$

and

$$\Gamma^{\text{inv}}(h_1 \rightarrow h_2 h_2) = \frac{(g_{h_1 h_2 h_2})^2}{16\pi m_{h_1}} \left(1 - \frac{4m_{h_2}^2}{m_{h_1}^2}\right)^{1/2}. \quad (30)$$

The invisible decay branching fraction of SM like scalar can be expressed as

$$\text{Br}_{\text{inv}} = \frac{\Gamma^{\text{inv}}}{\Gamma}. \quad (31)$$

We adopt the bounds on the invisible decay branching fraction for SM scalar to be $\text{Br}_{\text{inv}} \leq 24\%$ [75] (for $m_{h_1} \geq m_{H_0}/2$), the scalar mixing $\sin \theta \leq 0.4$ [76]-[78] and on the signal strength of SM Higgs $R_1 \geq 0.84$ [79, 80] from the LHC experiment results to constrain the model parameter space.

PLANCK constraint on relic density

The relic density of dark matter candidate H_0 must satisfy the PLANCK observational limit in order to be a viable candidate of dark matter. PLANCK observed relic density limit is given as with Ω_{DM} in the DM relic density normalised by the critical density of the Universe and h is the Hubble parameter normalised by a value of $100 \text{ Km s}^{-1} \text{ Mpc}^{-1}$ [63].

$$0.1172 \leq \Omega_{\text{DM}} h^2 \leq 0.1226. \quad (32)$$

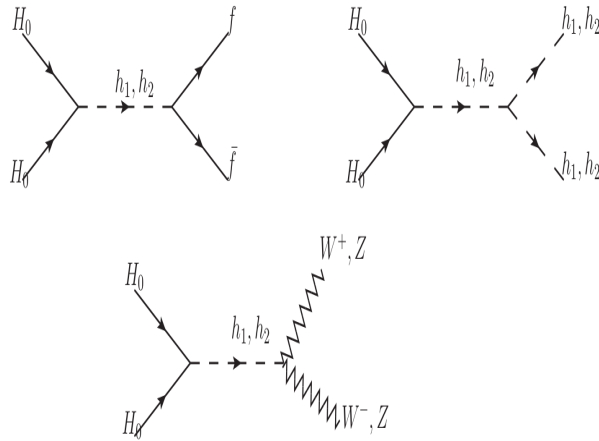


Figure 1: Feynman diagrams for the dominant annihilation channels of the dark matter candidate H_0 .

Direct Searches of Dark matter

Direct detection experiments of dark matter put an upper bound on dark matter nucleon elastic scattering cross-sections for different dark matter masses. In the present work, we consider the results of the following direct detection experiments of dark matter to constrain the model parameter space XENON-1T [64], PandaX-II [65], LUX [66] and DarkSide-50 [67].

4 Dark matter phenomenology

In this section we furnish the dark matter relic density and direct detection scattering cross-section formulas of the present extended inert doublet model with an additional real singlet scalar. These will be used to compute and constrain the model parameter space.

4.1 Relic Density

In order to calculate the dark matter relic density one needs to solve the Boltzmann equation which can be expressed as [81]

$$\frac{dn_{H_0}}{dt} + 3Hn_{H_0} = -\langle\sigma v\rangle [n_{H_0}^2 - (n_{H_0}^{\text{eq}})^2], \quad (33)$$

where n_{H_0} is the dark matter number density and $n_{H_0}^{\text{eq}}$ is the dark matter number density at thermal equilibrium. In Eq. (33) $\langle\sigma v\rangle$ is the thermal average total annihilation cross-section σ times the relative velocity v of the dark matter candidate H_0 and H is the Hubble parameter.

The expressions for $\langle\sigma v\rangle$ at a temperature T can be written as

$$\langle\sigma v\rangle = \frac{1}{8m_{H_0}^4 T K_2^2\left(\frac{m_{H_0}}{T}\right)} \int_{4m_{H_0}^2}^{\infty} ds (s - 4m_{H_0}^2) \sqrt{s} K_1\left(\frac{\sqrt{s}}{T}\right) \sigma(s), \quad (34)$$

where $\sigma(s)$ is the total annihilation cross-section of the dark matter particle H_0 , \sqrt{s} is the centre of mass energy, K_1 and K_2 are the first and second-order modified Bessel functions respectively. We calculate the total annihilation cross-sections of the dark matter candidate H_0 into final state SM particles (quarks, leptons, gauge bosons, Higgs boson) and also for the annihilation channels $H_0 H_0 \rightarrow h_2 h_2$ and $H_0 H_0 \rightarrow h_1 h_2$ mediated by both the particles h_1 and h_2 . The Feynman diagrams for the above-mentioned annihilation channels are shown in Figure 1 and the corresponding expressions for annihilation cross-sections are given in the appendix. Then the relic density of the dark matter candidate H_0 is computed using the expressions which are given as

$$\Omega_{\text{DM}} h^2 = 2.755 \times 10^8 \left(\frac{m_{H_0}}{\text{GeV}}\right) Y_0, \quad (35)$$

with

$$\frac{1}{Y_0} = \frac{1}{Y_F} + \left(\frac{45G}{\pi}\right)^{-\frac{1}{2}} \int_{T_0}^{T_F} g_*^{1/2} \langle\sigma v\rangle dT, \quad (36)$$

where Y_F is the value of Y at the freeze-out temperature T_F , G the universal gravitational constant, g_* is the degrees of freedom and T_0 is the temperature at the present epoch.

4.2 Direct detection

The dark matter particle H_0 interacts with the SM particles via Higgs exchange. The expression for the spin independent elastic scattering cross-section is given as

$$\sigma_{\text{SI}} = \frac{m_N^4}{\pi (m_{H_0} + m_N)^2} f^2 \left(\frac{\lambda_{h_1 H_0 H_0} \cos \theta}{m_{h_1}^2} + \frac{\lambda_{h_2 H_0 H_0} \sin \theta}{m_{h_2}^2} \right), \quad (37)$$

where m_N is the nucleon mass and f is the nucleon-Higgs form factor which has been approximated as 0.35 [82]. In Eq. (37) the couplings $\lambda_{h_1 H_0 H_0}$ and $\lambda_{h_2 H_0 H_0}$ can be written as

$$\lambda_{h_1 H_0 H_0} = \left(\frac{\lambda_L}{2} \cos \theta - \frac{\lambda_s}{2} \sin \theta \right), \quad (38)$$

$$\lambda_{h_2 H_0 H_0} = \left(\frac{\lambda_L}{2} \sin \theta + \frac{\lambda_s}{2} \cos \theta \right), \quad (39)$$

with

$$\lambda_L = \lambda_3 + \lambda_4 + \lambda_5 \text{ and } \lambda_s = \frac{\rho'_1 + 2\rho'_2 v_s}{v}. \quad (40)$$

In this work we consider various dark matter direct detection experiments bounds such as XENON-1T [64], PandaX-II [65], LUX [66] and DarkSide-50 [67] in order to constrain the model parameter space. We calculate the dark matter scattering cross-sections using Eqs. (37)-(40) and then compare it with the above mentioned experimental bounds.

4.3 Viable Model parameter space

In order to obtained viable model parameter space, we need to calculate relic density and direct detection scattering cross-section of a dark matter candidate H_0 . The relic density of H_0 as a function of dark matter mass is estimated from Eq. (35) by calculating the dark matter annihilation cross-sections for different annihilation channels given by Eqs. (63)-(68). Using Eq. (37), we compute the scattering cross-sections in direct detection of dark matter as a function of dark matter masses. With the theoretical bounds described in Section 3.1 they are then further constrained by the LEP and LHC bounds described in Section 3.2. We compute the relic density and direct detection scattering cross-section of the DM candidate for further constraining the model parameter space.

In left panels of Figures 2-5, the relic densities against the dark matter masses between 50 GeV to 500 GeV are plotted for chosen different sets of the free parameters. The free parameters in our model are m_{h_2} , v_s , θ , λ_L , λ_s , ρ_1 , ρ_3 , λ_2 . These parameters are chosen in such a manner that they are compatible with the bounds such as vacuum stability, pertubativity, LEP and LHC bounds. The relic densities are calculated and compared with the PLANCK results. The shadowed area bounded by two horizontal parallel lines in the left panels of Figures 2-5 show the PLANCK bounds where the calculated relic density is shown by the red lines. Further, direct detection scattering cross-sections, calculated with same sets of parameters used in the relic density plots (presented in left panels in Figures 2-5), are given in the right panels of Figures 2-5 for different dark matter masses ranging from 50 GeV to 500 GeV. Then we compared our direct detection scattering cross-sections obtained from (37) with the bounds from direct detection experiment such as XENON-1T, PandaX-II, LUX and DarkSide-50. Out of a large model parameter space, we selected four benchmark points (BPs) BP1-4 from Figures 2-5, given in Table 1, for calculating the GW intensity using the extended inert doublet dark matter model discussed in section 2. Table 1 shows the relic density ($\Omega_{\text{DM}}h^2$) and direct detection scattering cross-section (σ_{SI}) for each of the BPs. For a fixed value of DM mass, from the left panel of Figures 2-5, one can see certain dips in the relic density. This is due to the fact that when a new annihilation channel opens up the annihilation cross-section increases which in turn reduces the relic density. From the left panels of Figures 2-5, it is evident that when the DM mass (m_{H_0}) is close to $(m_{h_1}/2)$ and $m_{h_2}/2$, sudden reductions in the relic density occur. This is because

at these DM masses annihilation cross-sections increase significantly. For example, in case of $m_{h_2} = 150$ GeV sudden dip in the relic density for the dark matter mass close to 62.5 GeV and 75 GeV can be seen in left panel of Figure 2. In addition, dips in the relic density plot for DM masses close to m_W (mass of W boson), m_Z (mass of Z boson), m_{h_1} (mass of Higgs boson) and m_t (mass of top quark) can also be seen. At these DM masses, some new annihilation channels open up like $H_0H_0 \rightarrow W^+W^-$, $H_0H_0 \rightarrow ZZ$, $H_0H_0 \rightarrow h_1h_1$ and $H_0H_0 \rightarrow t\bar{t}$. Besides, when m_{H_0} is higher than $m_{h_2}/2$, relic density increases and becomes overabundant due to the decrease in the annihilation cross-section. As can be seen in the right panels of Figures 2-5, DM direct detection scattering cross-section (σ_{SI}) decreases as the DM mass increases. The right panel of Figures 2-5 show that the calculated σ_{SI} for four BPs are consistent with the bounds given by dark matter direct detection experiments like XENON-1T, LUX, PandaX-II and DarkSide-50. We checked that for high dark matter masses up to 1 TeV, the dark matter candidate H_0 also satisfies the measured relic abundance given by PLANCK. This can be achieved by considering high masses of m_{h_2} . Thus H_0 can be considered as a viable particle candidate of dark matter with the mass of the order of GeV - TeV.

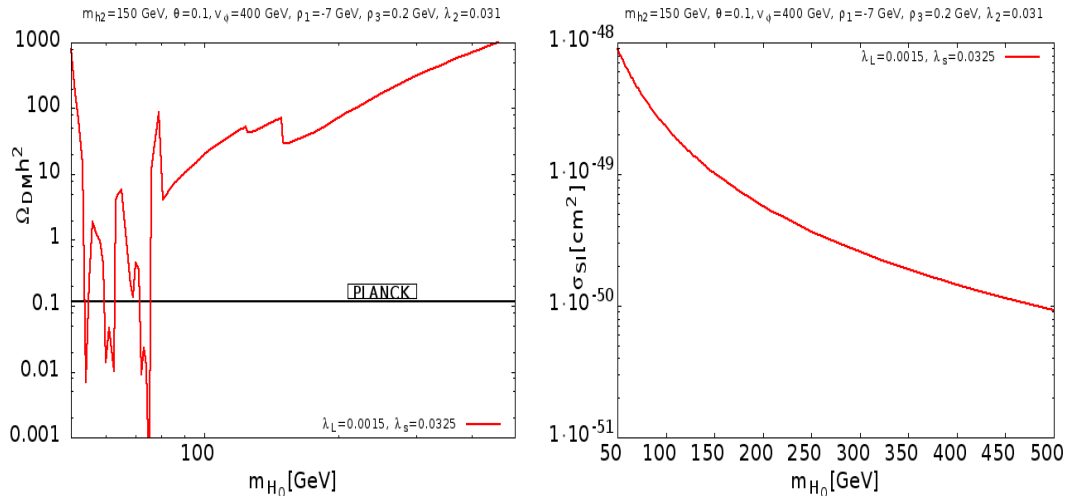


Figure 2: Variation of DM relic density as a function of DM mass m_{H_0} (left panel) and Variation of DM direct detection scattering cross-section as a function of DM mass m_{H_0} (right panel) for BP1. The parameter sets for BP1 are tabulated in Table 1.

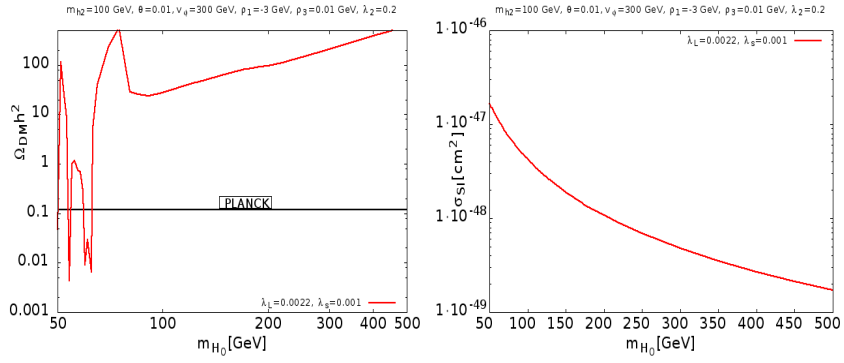


Figure 3: Same as in Figure 2 but for BP2.

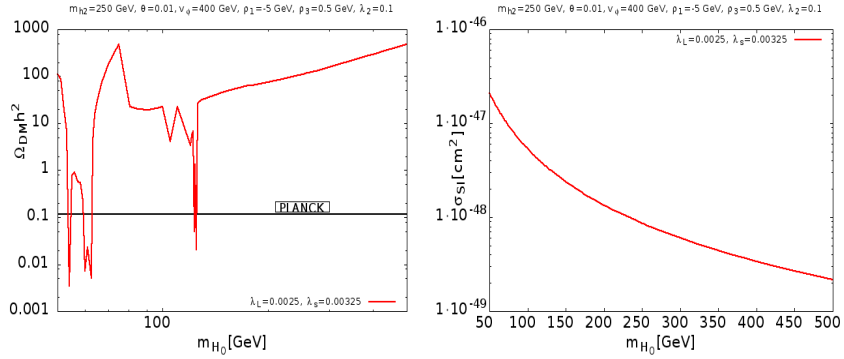


Figure 4: Same as in Figure 2 but for BP3.

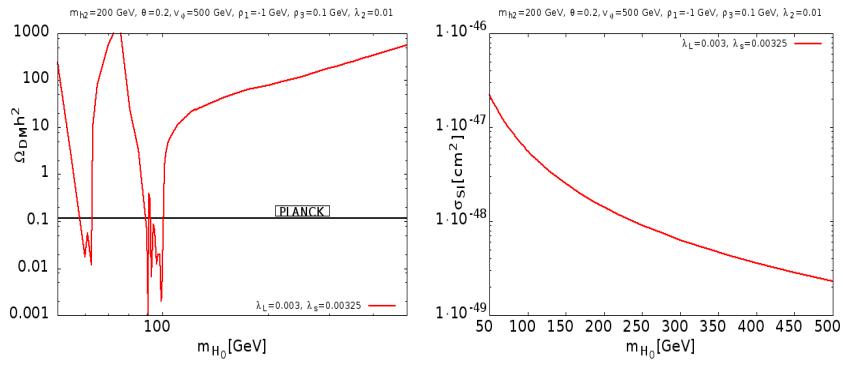


Figure 5: Same as in Figure 2 but for BP4.

5 Electroweak Phase transition and Gravitational Waves Production in Extended Inert Doublet Dark Matter Model

In this section we explore the electroweak phase transition and production of GWs from the considered dark matter model.

5.1 Effective Potential

To study the electroweak phase transition (EWPT) in the present model we add the finite temperature correction with the tree-level potential (Eq. (1)). Thus the finite temperature effective potential can be written as [83]

$$V_{\text{eff}} = V_{\text{tree-level}} + V_{1\text{-loop}}^{T=0} + V_{1\text{-loop}}^{T\neq0}, \quad (41)$$

where $V_{1\text{-loop}}^{T=0}$ and $V_{1\text{-loop}}^{T\neq0}$ are the one-loop corrected potential at zero temperature and at finite temperature respectively. The one-loop effective potential at zero temperature is given by

$$V_{1\text{-loop}}^{T=0} = \pm \frac{1}{64\pi^2} \sum_i n_i m_i^4 \left[\log \frac{m_i^2}{Q^2} - C_i \right], \quad (42)$$

where the ‘+’ sign is for bosons and ‘-’ sign is for fermions. Here, n_i is the number of degrees of freedom and m_i is the field-dependent masses of these particles. With $i = (h, H_0, A_0, H^\pm, s, W, Z, t)$. The degrees of freedom of these particle species are $n_W^\pm = 4$, $n_Z = 2$, $n_t = 12$ and $n_{h,H_0,A_0,H^\pm,s} = 1$. The quantity Q denotes the renormalisable scale which we take $Q = 246.22$ GeV in our calculations. In Eq. (42) C_i represents a numerical constant, for W, Z boson $C_{W,Z} = 5/6$ and for the other particles $C_{h,H_0,A_0,H^\pm,s,t} = 3/2$. The one-loop effective potential at finite temperature has the form

$$V_{1\text{-loop}}^{T\neq0} = \frac{T^2}{2\pi^2} \sum_i n_i J_\pm \left[\frac{m_i^2}{T^2} \right], \quad (43)$$

where

$$J_\pm \left(\frac{m_i^2}{T^2} \right) = \pm \int_0^\infty dy y^2 \log \left(1 \mp e^{-\sqrt{y^2 + \frac{m_i^2}{T^2}}} \right). \quad (44)$$

In this work we use the CosmoTransitions package [83] to compute the finite temperature correction of the tree-level potential.

5.2 Gravitational Waves Production from Dark Matter

The first-order cosmological phase transition originates from the bubble nucleation of a true vacuum state at a temperature known as the nucleation temperature at which the probability for a single bubble to nucleate within the horizon volume is of the order one. Initially, the bubbles are considered to have all possible shapes with different surface tension and internal pressure. The bubbles with the size just large enough for avoiding collapse are considered as a critical bubble. The bubbles which are smaller than the critical bubble tend to collapse whereas the larger bubbles tend to expand due to the pressure difference between the false and true vacua. During the collisions, the bubbles can not retain their spherical symmetry which initiates phase transitions and as a result, gravitational waves are produced.

The bubble nucleation rate per unit volume at a particular temperature can be written as [84]

$$\Gamma = \Gamma_0(T) e^{-S_3(T)/T} \quad (45)$$

where $\Gamma_0(T) \propto T^4$, $S_3(T)$ is the Euclidean action of the critical bubble. The Euclidean action $S_3(T)$ can be expressed as [84]

$$S_3 = 4\pi \int dr r^2 \left[\frac{1}{2} \left(\partial_r \vec{\phi} \right)^2 + V_{eff} \right], \quad (46)$$

where V_{eff} is the effective finite temperature potential represented in Eq. (41). Nucleation of the bubble occurs at the nucleation temperature T_n if it satisfies the condition $S_3(T_n)/T_n \approx 140$ [83].

The gravitational waves are produced from the first-order phase transition mainly by the three mechanisms such as bubble collisions [8]-[13], sound wave [14]-[17] and turbulence in the plasma [18]-[22]. The total GW intensity Ω_{GWh^2} as a function of frequency can be expressed as the sum of the contributions from the three components [8]-[22]

$$\Omega_{GWh^2} = \Omega_{col}h^2 + \Omega_{SWh^2} + \Omega_{turb}h^2. \quad (47)$$

The component from the bubbles collision $\Omega_{col}h^2$ is given by

$$\Omega_{col}h^2 = 1.67 \times 10^{-5} \left(\frac{\beta}{H} \right)^{-2} \frac{0.11v_w^3}{0.42 + v_w^2} \left(\frac{\kappa\alpha}{1 + \alpha} \right)^2 \left(\frac{g_*}{100} \right)^{-\frac{1}{3}} \frac{3.8 \left(\frac{f}{f_{col}} \right)^{2.8}}{1 + 2.8 \left(\frac{f}{f_{col}} \right)^{3.8}}, \quad (48)$$

with the parameter β

$$\beta = \left[HT \frac{d}{dT} \left(\frac{S_3}{T} \right) \right] \Big|_{T_n}, \quad (49)$$

where T_n is the nucleation temperature and H_n is the Hubble parameter at T_n . The most general expression of the bubble wall velocity has the form [85]

$$v_w = \frac{1/\sqrt{3} + \sqrt{\alpha^2 + 2\alpha/3}}{1 + \alpha}. \quad (50)$$

In some literatures, v_w is taken to be 1 (e.g. Ref. [37]) but we use the most general expression (Eq. (50)) for calculating the bubble wall velocity. The parameter κ in Eq. (48) represents the fraction of latent heat deposited in a thin shell which is given by

$$\kappa = 1 - \frac{\alpha_\infty}{\alpha}, \quad (51)$$

with

$$\alpha_\infty = \frac{30}{24\pi^2 g_*} \left(\frac{v_n}{T_n} \right)^2 \left[6 \left(\frac{M_W}{v} \right)^2 + 3 \left(\frac{M_Z}{v} \right)^2 + 6 \left(\frac{M_t}{v} \right)^2 \right], \quad (52)$$

In the above, v_n is the vacuum expectation value of Higgs at T_n and M_W , M_Z and M_t are the masses of W, Z and top quarks respectively. The parameter α is defined as the ratio of vacuum energy density ρ_{vac} released by the electroweak phase transition to the background energy density of the plasma ρ_*^{rad} at T_n . The expression of α has the form

$$\alpha = \left[\frac{\rho_{\text{vac}}}{\rho_*^{\text{rad}}} \right] \Big|_{T_n}. \quad (53)$$

with

$$\rho_{\text{vac}} = \left[\left(V_{\text{eff}}^{\text{high}} - T \frac{dV_{\text{eff}}^{\text{high}}}{dT} \right) - \left(V_{\text{eff}}^{\text{low}} - T \frac{dV_{\text{eff}}^{\text{low}}}{dT} \right) \right], \quad (54)$$

and

$$\rho_*^{\text{rad}} = \frac{g_* \pi^2 T_n^4}{30}. \quad (55)$$

The quantity f_{col} in Eq. (48) is the peak frequency produced by the bubble collisions which takes the form

$$f_{\text{col}} = 16.5 \times 10^{-6} \text{ Hz} \left(\frac{0.62}{v_w^2 - 0.1v_w + 1.8} \right) \left(\frac{\beta}{H} \right) \left(\frac{T_n}{100 \text{ GeV}} \right) \left(\frac{g_*}{100} \right)^{\frac{1}{6}}. \quad (56)$$

The sound wave (SW) component of the gravitational wave (Eq. (47)) is given by

$$\Omega_{\text{SW}} h^2 = 2.65 \times 10^{-6} \left(\frac{\beta}{H} \right)^{-1} v_w \left(\frac{\kappa_v \alpha}{1 + \alpha} \right)^2 \left(\frac{g_*}{100} \right)^{-\frac{1}{3}} \left(\frac{f}{f_{\text{SW}}} \right)^3 \left[\frac{7}{4 + 3 \left(\frac{f}{f_{\text{SW}}} \right)^2} \right]^{\frac{7}{2}}, \quad (57)$$

where κ_v is the fraction of latent heat transformed into the bulk motion of the fluid which has the following form

$$\kappa_v = \frac{\alpha_\infty}{\alpha} \left[\frac{\alpha_\infty}{0.73 + 0.083\sqrt{\alpha_\infty} + \alpha_\infty} \right]. \quad (58)$$

In Eq. (57) f_{SW} denotes the peak frequency produced by the sound wave mechanisms which takes the form

$$f_{\text{SW}} = 1.9 \times 10^{-5} \text{ Hz} \left(\frac{1}{v_w} \right) \left(\frac{\beta}{H} \right) \left(\frac{T_n}{100 \text{ GeV}} \right) \left(\frac{g_*}{100} \right)^{\frac{1}{6}}. \quad (59)$$

The component from the turbulence in the plasma $\Omega_{\text{turb}} h^2$ is given by

$$\Omega_{\text{turb}} h^2 = 3.35 \times 10^{-4} \left(\frac{\beta}{H} \right)^{-1} v_w \left(\frac{\epsilon \kappa_v \alpha}{1 + \alpha} \right)^{\frac{3}{2}} \left(\frac{g_*}{100} \right)^{-\frac{1}{3}} \frac{\left(\frac{f}{f_{\text{turb}}} \right)^3 \left(1 + \frac{f}{f_{\text{turb}}} \right)^{-\frac{11}{3}}}{\left(1 + \frac{8\pi f}{h_*} \right)}, \quad (60)$$

where $\epsilon = 0.1$ and f_{turb} denotes the peak frequency produced by the turbulence mechanism which can be written as

$$f_{\text{turb}} = 2.7 \times 10^{-5} \text{ Hz} \left(\frac{1}{v_w} \right) \left(\frac{\beta}{H} \right) \left(\frac{T_n}{100 \text{ GeV}} \right) \left(\frac{g_*}{100} \right)^{\frac{1}{6}}. \quad (61)$$

In Eq. (60) the parameter h_* has the following form

$$h_* = 16.5 \times 10^{-6} \text{ Hz} \left(\frac{T_n}{100 \text{ GeV}} \right) \left(\frac{g_*}{100} \right)^{\frac{1}{6}}. \quad (62)$$

In this work, Eqs. (47)-(62) are used for the computation of gravitational wave intensity.

5.3 Calculations and Results

The computation of GW intensity from the first order phase transition in the present particle DM model (inert doublet and a scalar singlet extended SM) has been performed for four chosen benchmark points for the model parameters. These are given in Table 1.

BP	m_{H_0} in GeV	m_{h_2} in GeV	v_s in GeV	θ	ρ_1 in GeV	ρ_3 in GeV	λ_L	λ_s	λ_2	$\Omega_{\text{DM}} h^2$	σ_{SI} cm 2
1	69	150	400	0.1	-7	0.2	0.0015	0.0325	0.031	0.1201	4.7463×10^{-49}
2	60	100	300	0.01	-3	0.01	0.0022	0.001	0.2	0.1190	1.1650×10^{-47}
3	125	250	400	0.01	-5	0.5	0.0025	0.00325	0.1	0.1188	3.4315×10^{-48}
4	92	200	500	0.2	-1	0.1	0.003	0.00325	0.01	0.1196	6.6464×10^{-48}

Table 1: The chosen four benchmarks points (BPs, BP1-4) to explore the GW production from an extended IDM with an additional real singlet scalar. The relic density and scattering cross-section values for each of the BPs are also mentioned in this Table.

BP	v_n in GeV	T_c in GeV	T_n in GeV	α	$\frac{\beta}{H}$
1	254.3189	129.2768	117.6208	0.4276	419.5639
2	252.4498	163.7417	151.9489	0.3267	425.6084
3	265.0494	130.0312	107.6148	0.5419	975.1794
4	171.5352	152.9061	137.1730	0.4030	1754.0734

Table 2: The values for the parameters used to calculate the GW intensity for each of the chosen BPs. See text for details.

We calculate gravitational wave intensity from the model and compare it with the sensitivity curves of different GW detectors such as BBO, eLISA, ALIA, DECIGO, U-DECIGO and aLIGO. The GW intensity depends mainly on factors like strength of the first-order phase transition (the parameter α), the time-scale of the phase transition (the parameter $1/\beta$), bubble wall velocity, nucleation temperature T_n and Higgs VEV v_n at the nucleation temperature T_n . In order to calculate the GW intensity, we first calculate the transition temperature of the first order phase transition. In calculating this, the finite temperature effective potential (Eqs. (41)-(44)) is first computed. For these calculations we use a publicly available package namely Cosmotransition package [83]. The tree-level potential (Eq. (1)) serves as an input to this package and provides the parameters related to the phase transition. The GW intensity is estimated by using Eqs. (47)-(62). In this work, we have selected four BPs (Table 1) such that they satisfy all constraints mentioned in section 3. The relic abundance $\Omega_{\text{DM}} h^2$ and the direct detection scattering cross-section σ_{SI} obtained from each of the four BPs are also given in Table 1.

In Figure 6 we show the phase transition properties for BP1. The left and right panels of Figure 6 show the phase structure of the model and the tunnelling profile as a function of the bubble radius respectively. As can be seen in the left panel of Figure 6, there exists

two transition temperatures at $T_n = 117.6208$ GeV and $T = 238.2557$ GeV. We only consider the low-temperature phase transition because the low nucleation temperature is more sensitive to probe the GW signal. An electroweak phase transition occurs when the temperature of the Universe drops which results in a separation of potential between a high phase and a low phase by a potential barrier. In this case, a first-order phase transition occurs at the nucleation temperature $T_n = 117.6208$ GeV.

The phase transition properties for BP2, BP3 and BP4 are also studied but no significant differences from BP1 are noted. We furnish the parameters $(\alpha, \beta/H, T_n, v_n)$ used in the calculation of the GW intensity for all BPs in Table 2. From Table 2, one can see that the nucleation temperature T_n is smaller than the critical temperature T_c (the temperature at which there exist two degenerate minima separated by a potential barrier) for each of the BPs. Figure 7 shows the variation of Gravitational wave intensity as a function of the GW frequency for all of the BPs (BP1-BP4). For different BPs, GW intensities attain peaks at different frequencies (Figure 7). The peak of the GW intensity for BP1, BP2, BP3, and BP4 appears at frequency 2.0989×10^{-3} Hz, 2.7982×10^{-3} Hz, 4.2967×10^{-3} Hz and 10^{-2} Hz respectively. We obtained higher GW intensity for BP1 as compared to the other BPs. In Figure 7, we also plot the GW intensity of four BPs along with the sensitivity curves of GW detectors (BBO, eLISA, ALIA, DECIGO, U-DECIGO, aLIGO and LISA). As seen from Figure 7 the GW intensity for all four of the BPs (BP1, BP2, BP3 and BP4) fall within the sensitivity curves of the N2A5M5L6 configuration of eLISA, BBO and U-DECIGO. However, BP1 is special because it shows higher intensity than the rest of the cases. It may be inferred from Figure 7 and Table 2, the GW intensity mainly depends on β . Table 2 shows that for BP1, the value of the parameter β is the smallest and the corresponding GW intensity is the highest along with the lowest peak frequency at 2.0989×10^{-3} .

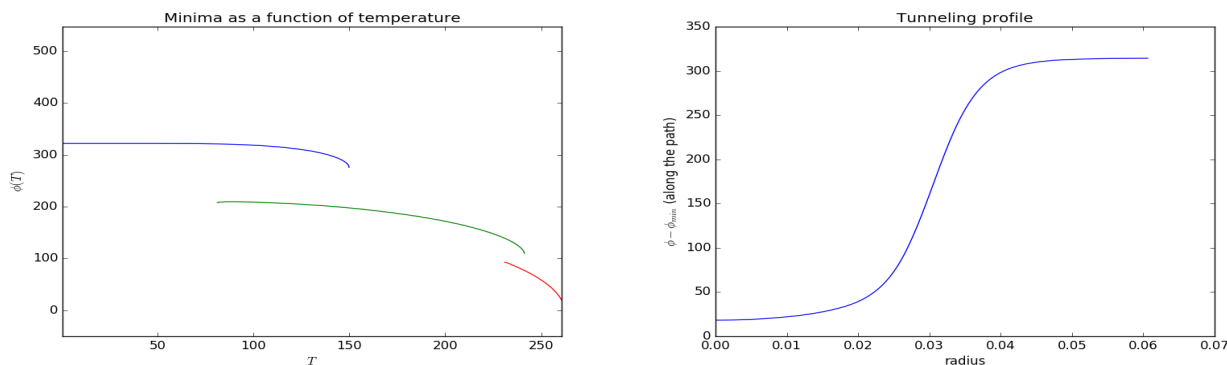


Figure 6: Phase transition properties for the BP1. The left panel is for the position of the minima as a function of temperature and the right panel is for the tunnelling profile as a function of bubble radius.

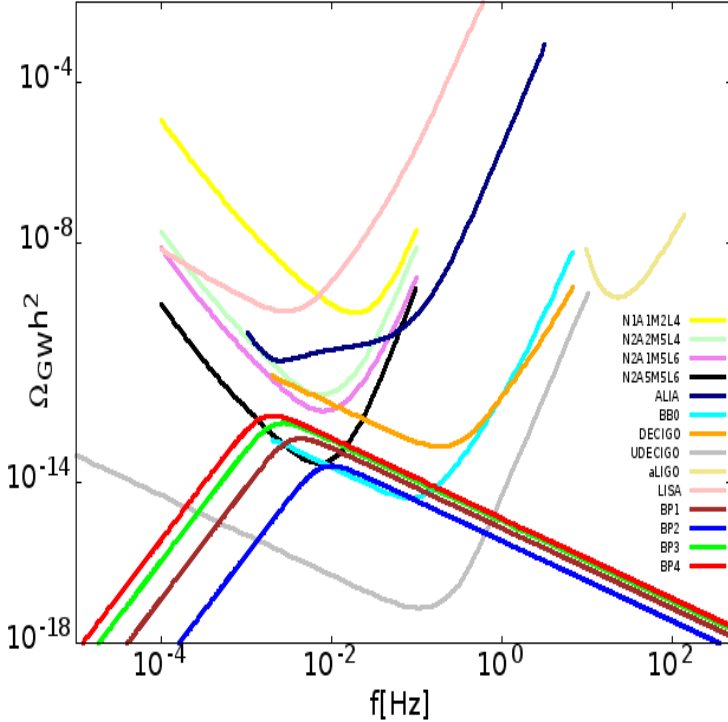


Figure 7: Comparision of the chosen four BPs with the sensitivity curves of N1A1M2L4, N2A2M5L4, N2A1M5L6 and N2A5M5L6 configurations of eLISA, ALIA, BBO, DECIGO, U-DECIGO, aLIGO and LISA detectors.

6 Summary and Conclusions

In this work, we have explored the possible production mechanisms of GW from the first-order phase transition of the early Universe and presented its detectability with the future space-based GW detectors (BBO, eLISA, ALIA, DECIGO, U-DECIGO and aLIGO). We discussed the phase transition properties in details by considering an extended inert doublet model with an additional real singlet scalar. A discrete Z_2 symmetry has been imposed on the potential which made the lightest stable inert particle a viable particle candidate of dark matter. Due to the imposition of this Z_2 symmetry inert particle does not interact with the SM particles and also it does not acquire any VEV. The added real singlet scalar acquires a VEV and it mixes with the SM Higgs which resulted in two new physical scalars h_1 and h_2 . Here we considered h_1 as the SM like Higgs boson and the other scalar h_2 as the added physical scalar. We constrain the model parameters from vacuum stability, perturbativity, LEP and LHC bounds, relic density as measured by PLANCK and the bounds from the direct detection experiments such as XENON-1T, PandaX-II, LUX and

DarkSide-50. The model parameter space thus constrained. We choose four benchmark points from the constrained parameter space for the computation of GW intensity and explore the GW production from the first-order phase transition of the tree-level potential. We included the finite temperature corrections of the tree-level potential. We calculated the GW intensity for four BPs and found that the GW signals are detectable by the following future generation detectors: BBO, U-DECIGO and eLISA (configuration - N2A5M5L6). It has been found that the GW intensity increases as β decreases. In addition, the lower value of β also lowers the frequency at which the maximum GW intensity is produced. In this work, we have successfully established that the extended inert doublet model under consideration can explain the dark matter as well as the strong first-order electroweak phase transition. This implies that the properties of dark matter can be extensively studied through indirect detection of dark matter via detection of GW signals with the future detectors.

Appendix

In this work, we derive the following expressions of annihilation cross-sections for the possible annihilation channels of the inert dark matter candidate.

$$\sigma (H_0 H_0 \rightarrow f \bar{f}) = \frac{N_c}{2\pi} m_f^2 \left(\frac{s}{s - 4m_{H_0}^2} \right)^{1/2} \left(1 - \frac{4m_f^2}{s} \right)^{3/2} \left(\frac{(\lambda_{h_1 H_0 H_0})^2 \cos^2 \theta}{(s - m_{h_1}^2)^2 + m_{h_1}^2 \Gamma_{h_1}^2} \right. \\ \left. + \frac{(\lambda_{h_2 H_0 H_0})^2 \sin^2 \theta}{(s - m_{h_2}^2)^2 + m_{h_2}^2 \Gamma_{h_2}^2} + \frac{2 \sin \theta \cos \theta \lambda_{h_1 H_0 H_0} \lambda_{h_2 H_0 H_0} ((s - m_{h_1}^2)(s - m_{h_2}^2) + m_{h_1} m_{h_2} \Gamma_{h_1} \Gamma_{h_2})}{((s - m_{h_1}^2)^2 + m_{h_1}^2 \Gamma_{h_1}^2)((s - m_{h_2}^2)^2 + m_{h_2}^2 \Gamma_{h_2}^2)} \right), \quad (63)$$

$$\sigma (H_0 H_0 \rightarrow W^+ W^-) = \frac{1}{\pi s} \left(\frac{s}{s - 4m_{H_0}^2} \right)^{1/2} \left(1 - \frac{4m_W^2}{s} \right)^{1/2} \left(2 + \frac{(s - 2m_W^2)^2}{4m_W^4} \right) \left(\frac{m_W^2}{v_H} \right)^2 \\ \left(\frac{(g_{h_1 H_0 H_0})^2 \cos^2 \theta}{(s - m_{h_1}^2)^2 + m_{h_1}^2 \Gamma_{h_1}^2} + \frac{(g_{h_2 H_0 H_0})^2 \sin^2 \theta}{(s - m_{h_2}^2)^2 + m_{h_2}^2 \Gamma_{h_2}^2} \right. \\ \left. + \frac{2 \sin \theta \cos \theta g_{h_1 H_0 H_0} g_{h_2 H_0 H_0} ((s - m_{h_1}^2)(s - m_{h_2}^2) + m_{h_1} m_{h_2} \Gamma_{h_1} \Gamma_{h_2})}{((s - m_{h_1}^2)^2 + m_{h_1}^2 \Gamma_{h_1}^2)((s - m_{h_2}^2)^2 + m_{h_2}^2 \Gamma_{h_2}^2)} \right), \quad (64)$$

$$\begin{aligned}
\sigma(H_0 H_0 \rightarrow ZZ) = & \frac{1}{2\pi s} \left(\frac{s}{s - 4m_{H_0}^2} \right)^{1/2} \left(1 - \frac{4m_Z^2}{s} \right)^{1/2} \left(2 + \frac{(s - 2m_Z^2)^2}{4m_Z^4} \right) \left(\frac{m_Z^2}{v_H} \right)^2 \\
& \left(\frac{(g_{h_1 H_0 H_0})^2 \cos^2 \theta}{(s - m_{h_1}^2)^2 + m_{h_1}^2 \Gamma_{h_1}^2} + \frac{(g_{h_2 H_0 H_0})^2 \sin^2 \theta}{(s - m_{h_2}^2)^2 + m_{h_2}^2 \Gamma_{h_2}^2} \right. \\
& \left. + \frac{2 \sin \theta \cos \theta g_{h_1 H_0 H_0} g_{h_2 H_0 H_0} ((s - m_{h_1}^2)(s - m_{h_2}^2) + m_{h_1} m_{h_2} \Gamma_{h_1} \Gamma_{h_2})}{((s - m_{h_1}^2)^2 + m_{h_1}^2 \Gamma_{h_1}^2)((s - m_{h_2}^2)^2 + m_{h_2}^2 \Gamma_{h_2}^2)} \right), \tag{65}
\end{aligned}$$

$$\begin{aligned}
\sigma(H_0 H_0 \rightarrow h_1 h_1) = & \frac{1}{\pi s} \left(\frac{s}{s - 4m_{H_0}^2} \right)^{1/2} \left(1 - \frac{4m_{h_1}^2}{s} \right)^{1/2} \left(\frac{(g_{h_1 H_0 H_0})^2 (g_{h_1 h_1 h_1})^2}{(s - m_{h_1}^2)^2 + m_{h_1}^2 \Gamma_{h_1}^2} \right. \\
& \left. + \frac{(g_{h_2 H_0 H_0})^2 (g_{h_2 h_1 h_1})^2}{(s - m_{h_2}^2)^2 + m_{h_2}^2 \Gamma_{h_2}^2} \right. \\
& \left. + \frac{2 (g_{h_1 H_0 H_0}) (g_{h_2 H_0 H_0}) (g_{h_1 h_1 h_1}) (g_{h_2 h_1 h_1}) ((s - m_{h_1}^2)(s - m_{h_2}^2) + m_{h_1} m_{h_2} \Gamma_{h_1} \Gamma_{h_2})}{((s - m_{h_1}^2)^2 + m_{h_1}^2 \Gamma_{h_1}^2)((s - m_{h_2}^2)^2 + m_{h_2}^2 \Gamma_{h_2}^2)} \right), \tag{66}
\end{aligned}$$

$$\begin{aligned}
\sigma(H_0 H_0 \rightarrow h_2 h_2) = & \frac{1}{\pi s} \left(\frac{s}{s - 4m_{H_0}^2} \right)^{1/2} \left(1 - \frac{4m_{h_2}^2}{s} \right)^{1/2} \left(\frac{(g_{h_1 H_0 H_0})^2 (g_{h_1 h_2 h_2})^2}{(s - m_{h_1}^2)^2 + m_{h_1}^2 \Gamma_{h_1}^2} \right. \\
& \left. + \frac{(g_{h_2 H_0 H_0})^2 (g_{h_2 h_2 h_2})^2}{(s - m_{h_2}^2)^2 + m_{h_2}^2 \Gamma_{h_2}^2} \right. \\
& \left. + \frac{2 (g_{h_1 H_0 H_0}) (g_{h_2 H_0 H_0}) (g_{h_1 h_2 h_2}) (g_{h_2 h_2 h_2}) ((s - m_{h_1}^2)(s - m_{h_2}^2) + m_{h_1} m_{h_2} \Gamma_{h_1} \Gamma_{h_2})}{((s - m_{h_1}^2)^2 + m_{h_1}^2 \Gamma_{h_1}^2)((s - m_{h_2}^2)^2 + m_{h_2}^2 \Gamma_{h_2}^2)} \right), \tag{67}
\end{aligned}$$

$$\begin{aligned}
\sigma(H_0 H_0 \rightarrow h_1 h_2) = & \frac{1}{4\pi s} \left(\frac{s}{s - 4m_{H_0}^2} \right)^{1/2} \left(1 - \frac{4(m_{h_1} + m_{h_2})^2}{s} \right)^{1/2} \left(1 - \frac{4(m_{h_1} - m_{h_2})^2}{s} \right)^{1/2} \\
& \left(\frac{(g_{h_1 H_0 H_0})^2 (g_{h_2 h_1 h_1})^2}{(s - m_{h_1}^2)^2 + m_{h_1}^2 \Gamma_{h_1}^2} + \frac{(g_{h_2 H_0 H_0})^2 (g_{h_1 h_2 h_2})^2}{(s - m_{h_2}^2)^2 + m_{h_2}^2 \Gamma_{h_2}^2} \right. \\
& \left. + \frac{2 (g_{h_1 H_0 H_0}) (g_{h_2 H_0 H_0}) (g_{h_2 h_1 h_1}) (g_{h_1 h_2 h_2}) ((s - m_{h_1}^2)(s - m_{h_2}^2) + m_{h_1} m_{h_2} \Gamma_{h_1} \Gamma_{h_2})}{((s - m_{h_1}^2)^2 + m_{h_1}^2 \Gamma_{h_1}^2)((s - m_{h_2}^2)^2 + m_{h_2}^2 \Gamma_{h_2}^2)} \right). \tag{68}
\end{aligned}$$

The expressions for the couplings are given in the following

$$g_{h_1 H_0 H_0} = \left(\frac{\lambda_L}{2} \cos \theta - \frac{\lambda_s}{2} \sin \theta \right) v = \lambda_{h_1 H_0 H_0} v, \tag{69}$$

$$g_{h_2 H_0 H_0} = \left(\frac{\lambda_L}{2} \sin \theta + \frac{\lambda_s}{2} \cos \theta \right) v = \lambda_{h_2 H_0 H_0} v, \quad (70)$$

$$g_{h_1 h_2 h_2} = \frac{1}{2} (6\lambda_1 v \cos \theta \sin^2 \theta + 2\rho_1 \cos^2 \theta \sin \theta - \rho_1 \sin^3 \theta + 2v\rho_2 \cos^3 \theta - 4v\rho_2 \cos \theta \sin^2 \theta + 4v_s \rho_2 \cos^2 \theta \sin \theta - 2v_s \rho_2 \sin^3 \theta - 2\rho_3 \cos^2 \theta \sin \theta - 6v_s \rho_4 \cos^2 \theta \sin \theta), \quad (71)$$

$$g_{h_2 h_1 h_1} = \frac{1}{2} (6\lambda_1 v \cos^2 \theta \sin \theta - 2\rho_1 \cos \theta \sin^2 \theta + \rho_1 \cos^3 \theta + 2v\rho_2 \sin^3 \theta - 4v\rho_2 \cos^2 \theta \sin \theta - 4v_s \rho_2 \cos \theta \sin^2 \theta + 2v_s \rho_2 \cos^3 \theta + 2\rho_3 \cos \theta \sin^2 \theta + 6v_s \rho_4 \cos \theta \sin^2 \theta), \quad (72)$$

$$g_{h_1 h_1 h_1} = (v\lambda_1 \cos^3 \theta - \frac{1}{2}\rho_1 \sin \theta \cos^2 \theta + v\rho_2 \sin^2 \theta \cos \theta - v_s \rho_2 \sin \theta \cos^2 \theta - \frac{1}{3}\rho_3 \sin^3 \theta - v_s \rho_4 \sin^3 \theta), \quad (73)$$

$$g_{h_2 h_2 h_2} = (v\lambda_1 \sin^3 \theta + \frac{1}{2}\rho_1 \sin^2 \theta \cos \theta + v\rho_2 \cos^2 \theta \sin \theta + v_s \rho_2 \sin^2 \theta \cos \theta + \frac{1}{3}\rho_3 \cos^3 \theta + v_s \rho_4 \cos^3 \theta). \quad (74)$$

References

- [1] Virgo, LIGO Scientific Collaboration, B. P. Abbott et al., Phys. Rev. Lett. **116**, 241103 (2016).
- [2] VIRGO, LIGO Scientific Collaboration, B. P. Abbott et al., Phys. Rev. Lett. **118**, 221101, (2017).
- [3] A. Vilenkin and E. P. S. Shellard, Cosmic Strings and Other Topological Defects. Cambridge University Press, 2000. <https://www.cambridge.org/mw/academic/subjects/physics/theoretical-physics-and-mathematical-physics/cosmic-strings-and-other-topological-defects?format=PB>.
- [4] A. A. Starobinsky, JETP Lett. **30**, 682 (1979).
- [5] S. Y. Khlebnikov and I. I. Tkachev, Phys. Rev. D **56**, 653 (1997).
- [6] E. Witten, Phys. Rev. D **30**, 272 (1984).
- [7] C. J. Hogan, Mon. Not. Roy. Astron. Soc. **218**, 629 (1986).

- [8] A. Kosowsky, M. S. Turner and R. Watkins, Phys. Rev. D **45**, 4514 (1992).
- [9] A. Kosowsky and M. S. Turner, Phys. Rev. D **47**, 4372 (1993).
- [10] S. J. Huber and T. Konstandin, JCAP **09**, 022 (2008).
- [11] A. Kosowsky, M. S. Turner and R. Watkins, Phys. Rev. Lett. **69**, 2026 (1992).
- [12] M. Kamionkowski, A. Kosowsky and M. S. Turner, Phys. Rev. D **49**, 2837 (1994). [astro-ph/9310044].
- [13] C. Caprini, R. Durrer and G. Servant, Phys. Rev. D **77**, 124015 (2008). [astro-ph]].
- [14] M. Hindmarsh, S. J. Huber, K. Rummukainen and D. J. Weir, Phys. Rev. Lett. **112**, 041301 (2014).
- [15] J. T. Giblin, Jr. and J. B. Mertens, JHEP **12**, 042 (2013).
- [16] J. T. Giblin and J. B. Mertens, Phys. Rev. D **90**, 023532 (2014).
- [17] M. Hindmarsh, S. J. Huber, K. Rummukainen and D. J. Weir, Phys. Rev. D **92**, 123009 (2015).
- [18] C. Caprini and R. Durrer, Phys. Rev. D **74**, 063521 (2006).
- [19] T. Kahnashvili, A. Kosowsky, G. Gogoberidze and Y. Maravin, Phys. Rev. D **78**, 043003 (2008).
- [20] T. Kahnashvili, L. Campanelli, G. Gogoberidze, Y. Maravin and B. Ratra, Phys. Rev. D **78**, 123006 (2008), Erratum: [Phys. Rev. D **79**, 109901 (2009)].
- [21] T. Kahnashvili, L. Kisslinger and T. Stevens, Phys. Rev. D **81**, 023004 (2010).
- [22] C. Caprini, R. Durrer and G. Servant, JCAP **12**, 024 (2009).
- [23] K. Kajantie, M. Laine, K. Rummukainen, and M. E. Shaposhnikov, Phys. Rev. Lett. **77**, 2887 (1996).
- [24] M. Gurtler, E.-M. Ilgenfritz, and A. Schiller, Phys. Rev. D **56**, 3888 (1997).
- [25] F. Csikor, Z. Fodor, and J. Heitger, Phys. Rev. Lett. **82**, 21 (1999).
- [26] D. Land and E. D. Carlson, Phys. Lett. B **292**, 107 (1992).

[27] A. Hammerschmitt, J. Kripfganz, and M. G. Schmidt, *Z. Phys. C* **64**, 105 (1994).

[28] H. H. Patel and M. J. Ramsey-Musolf, *Phys. Rev. D* **88**, 035013 (2013).

[29] W. Huang, Z. Kang, J. Shu, P. Wu, and J. M. Yang, *Phys. Rev. D* **91**, 025006 (2015).

[30] N. Blinov, J. Kozaczuk, D. E. Morrissey, and C. Tamarit, *Phys. Rev. D* **92**, 035012 (2015).

[31] J. Kozaczuk, S. Profumo, L. S. Haskins and C. L. Wainwright, *JHEP* **01**, 144 (2015).

[32] V. Vaskonen, *Phys. Rev. D* **95**, no. 12, 123515 (2017).

[33] W. Chao, H. K. Guo and J. Shu, *JCAP* **09**, no. 09, 009 (2017).

[34] T. Hasegawa, N. Okada and O. Seto, *Phys. Rev. D* **99**, 095039 (2019).

[35] M. Artymowski, M. Lewicki and J. D. Wells, *JHEP* **03**, 066 (2017).

[36] P. S. B. Dev, F. Ferrer, Y. Zhang and Y. Zhang, arXiv:1905.00891 [hep-ph].

[37] V. R. Shajiee and A. Tofighi, *Eur. Phys. J. C* **79**, 360 (2019).

[38] F. P. Huang and J. H. Yu, *Phys. Rev. D* **98**, 095022 (2018).

[39] A. Paul, D. Majumdar and A. Dutta Banik, *JCAP* **05**, 029 (2019).

[40] A. Dutta Banik, D. Majumdar and A. Biswas, *Eur. Phys. J. C* **76**, 346 (2016).

[41] A. Biswas, D. Majumdar and P. Roy, *JHEP* **04**, 065 (2015).

[42] A. Biswas, D. Majumdar, A. Sil and P. Bhattacharjee, *JCAP* **12**, 049 (2013).

[43] C. E. Yaguna, *JHEP* **08**, 060 (2011).

[44] E. Molinaro, C. E. Yaguna and O. Zapata, *JCAP* **07**, 015 (2014).

[45] R. D. Peccei, *Lect. Notes Phys.* **741**, 3 (2008).

[46] S. Weinberg, *Phys. Rev. Lett.* **40**, 223 (1978).

[47] A. Paul, D. Majumdar and K. Prasad Modak, *Pramana* **92**, 44 (2019).

[48] G. Jungman, M. Kamionkowski and K. Griest, *Phys. Rept.* **267**, 195 (1996).

[49] A. Lidz and L. Hui, *Phys. Rev. D* **98**, 023011 (2018).

- [50] N. C. Amorisco and A. Loeb, arXiv:1808.00464 [astro-ph.GA].
- [51] L. Bergstrom, M. Fairbairn and L. Pieri, Phys. Rev. D **74**, 123515 (2006).
- [52] E. Ma, Phys. Rev. D **73**, 077301 (2006).
- [53] L. Lopez Honorez, E. Nezri, J.F. Oliver, M.H.G. Tytgat, JCAP **02**, 028 (2007).
- [54] D. Majumdar, A. Ghosal, Mod. Phys. Lett. A **23**, 2011 (2008). arXiv:hep-ph/0607067
- [55] M. Gustafsson, E. Lundstrom, L. Bergstrom, J. Edsjo, Phys. Rev. Lett. **99**, 041301 (2007).
- [56] M. Aoki, S. Kanemura and H. Yokoya, Phys. Lett. B **725**, 302 (2013).
- [57] Q.-H. Cao, E. Ma, G. Rajasekaran, Phys. Rev. D **76**, 095011 (2007).
- [58] L. Lopez Honorez, C.E. Yaguna, JCAP **01**, 002 (2011).
- [59] A. Dutta Banik and D. Majumdar, Eur. Phys. J. C **74**, 3142 (2014).
- [60] A. Dutta Banik and D. Majumdar, Phys. Lett. B **743**, 420 (2015).
- [61] K. Kannike, Eur. Phys. J. C **72**, 2093 (2012).
- [62] J. Beringer et al. (Particle Data Group), Phys. Rev. D **86**, 010001 (2012)
- [63] P. A. R. Ade *et al.* [Planck Collaboration], Astron. Astrophys. **571**, A16 (2014).
- [64] E. Aprile *et al.* [XENON Collaboration], JCAP **1604**, 027 (2016).
- [65] A. Tan *et al.* [PandaX-II Collaboration], Phys. Rev. Lett. **117**, 121303 (2016).
- [66] D. S. Akerib *et al.* [LUX Collaboration], Phys. Rev. Lett. **118**, 021303 (2017).
- [67] L. Marini *et al.* [DarkSide Collaboration], Nuovo Cim. C **39**, 247 (2016).
- [68] V. Corbin and N. J. Cornish, Class. Quant. Grav. **23**, 2435 (2006) .
- [69] C. J. Moore, R. H. Cole, and C. P. L. Berry, Class. Quant. Grav. **32**, 015014 (2015).
- [70] X. Gong et al., J. Phys. Conf. Ser. **610**, 012011 (2015).
- [71] M. Musha [DECIGO Working group], Proc. SPIE Int. Soc. Opt. Eng. **10562**, 105623T (2017).

- [72] H. Kudoh, A. Taruya, T. Hiramatsu and Y. Himemoto, Phys. Rev. D **73**, 064006 (2006).
- [73] [LIGO Scientific Collaboration], arXiv:1904.03187 [gr-qc].
- [74] C. Patrignani *et al.* [Particle Data Group], Chin. Phys. C **40**, 100001 (2016).
- [75] CERN Technical Report No. CMS-PAS-HIG-16-016 (2016).
- [76] T. Robens and T. Stefaniak, Eur. Phys. J. C **75**, 104 (2015).
- [77] K. Cheung, P. Ko, J. S. Lee, and P. Y. Tseng, J. High Energy Phys. **10**, 057 (2015).
- [78] G. Dupuis, J. High Energy Phys. **07**, 008 (2016).
- [79] V. Khachatryan et al. (CMS Collaboration), Eur. Phys. J. C **75**, 212 (2015).
- [80] G. Aad et al. (ATLAS Collaboration), Eur. Phys. J. C **76**, 6 (2016).
- [81] E. W. Kolb and M. S. Turner, Front. Phys. **69**, 1 (1990).
- [82] J. M. Cline, K. Kainulainen, P. Scott and C. Weniger, Phys. Rev. D **88**, 055025 (2013), Erratum: Phys. Rev. D **92**, 039906 (2015).
- [83] C. L. Wainwright, Comput. Phys. Commun. **183**, 2006 (2012).
- [84] A. D. Linde, Nucl. Phys. B **216**, 421 (1983).
- [85] P. J. Steinhardt, Phys. Rev. D **25**, 2074 (1982).